Journal of Structural Geology 31 (2009) 491–497

Contents lists available at ScienceDirect

Journal of Structural Geology

journal homepage: www.elsevier.com/locate/jsg

# Influence of an inhomogeneous stress field and fault-zone thickness on the displacements and stresses induced by normal faulting

Yijie Zhou [a,b], Caibo Hu [a,b], Yongen Cai [a,b,*]

[a] Department of Geophysics, Peking University, #5 Yiheyuan Road, Haidian, Beijing 100871, China
[b] PKU-CEA Joint Research Center in Modern Seismology, #5 Yiheyuan Road, Haidian, Beijing 100871, China

ARTICLE INFO

*Article history:*
Received 17 July 2008
Received in revised form
3 March 2009
Accepted 16 March 2009
Available online 15 April 2009

*Keywords:*
FEM
Normal fault
Failure regions
Inhomogeneous stress field

ABSTRACT

We used the finite element method (FEM) to simulate the temporal evolution of an inhomogeneous stress field with the aim of investigating the displacement and stress fields induced by slip upon a normal fault zone with a given thickness. The modeling results reveal: 1) the site of maximum slip is along the lower part of the fault, not near the surface, and the locations upon the fault of maximum shear stress drop and maximum slip do not coincide; 2) the maximum horizontal and vertical displacements at the ground surface are located at some distance from the fault trace; and 3) slip of the fault may result in two failure regions near the ground surface: one close to the surface trace of the fault, and the other within the hanging wall at some distance from the fault; it is in the regions that a succession of normal faults is typically observed in geological examples. These results differ from those obtained using seismic dislocation theory in semi-infinite space, where the effects of the inhomogeneous stress field and thickness of the fault zone are not considered.



## 1. Introduction

The observed slip on a fault, as measured during a geological survey, is the sum total of numerous small displacements related to earthquakes and other geological events. Ground surface deformation features and fault slip can be attributed to the displacements and stress fields induced by earth movements. The displacement field is related to rock properties, the tectonic stress field, fault geometry, and the pattern of fault failure. In seismology, the dislocation theory based on homogeneous, isotropic elastic semi-infinite space is used to study displacements and stress fields caused by dislocations on the fault, specified in advance. The theory can provide analytical solutions regarding the displacement and stress field (e.g., Chinnery, 1963; Manshinha and Smylie, 1971; Okada, 1985, 1992), and the solutions are helpful in understanding the deformation characteristics of the ground surface. However, the theory cannot predict the displacements and stress fields caused by movements within a thick and complex fault zone if the tectonic stress field is inhomogeneous and the material is heterogeneous.

Numerous geological examples show that faults are usually part of a thick zone that can be divided into three primary regions: the fault core, the damage zone, and the protolith. The thickness of the zone may vary from tens to thousands of meters (e.g., Evans, 1990; Caine et al., 1996; Schulz and Evans, 2000). Li et al. (1994, 1999) and Li (2003) reported that the Landers Fault Zone is about 100–200 m thick, as obtained by the study of trapped waves.

The tectonic stress field is not only related to gravity and plate-boundary forces (Zoback, 1992), but also to earthquakes (Hauksson, 1994; Day et al., 1998), geological structures (Colmenares and Zoback, 2003; Roman et al., 2004; Tamagawa and Pollard, 2008), geothermic anomaly (Aagaard et al., 2001; Xu et al., 2005), rock heterogeneities, layering (Gudmundsson, 2006), and so on. There is no doubt that the inhomogeneous nature of the stress field and thickness of the fault zone are two important factors affecting fault slip, but it is difficult to find analytical solutions that take these factors into account; even the relevant numerical solutions are rarely investigated.

This paper uses the results of a finite element method (FEM) analysis to evaluate the influence of an inhomogeneous stress field on the displacement and stress fields induced by slip along a normal fault, taking into account the thickness of the fault zone.

## 2. Simulation of fault slip by FEM

The total slip along a fault is the sum total of numerous small slips produced during many earthquakes. To understand the characteristics of ground surface deformation and failure, it is necessary to study the displacements and stress fields related to this slip. Slip upon a fault is the result of softening of material in the fault zone,

* Corresponding author. Department of Geophysics, Peking University, #5 Yiheyuan Road, Haidian, Beijing 100871, China. Tel.: +86 010 62755441; fax: +86 010 62751159.
*E-mail address:* yongen@pku.edu.cn (Y. Cai).

0191-8141/$ – see front matter © 2009 Elsevier Ltd. All rights reserved.
doi:10.1016/j.jsg.2009.03.018

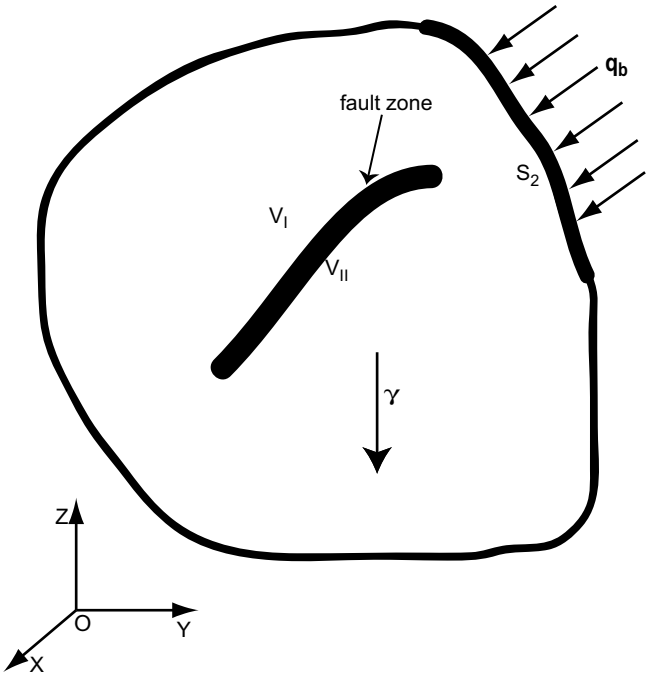


**Fig. 1.** Sketch of the employed mechanical model. The region to be studied (i.e., the region enclosed by the thin line) is divided into two domains ($V_I$ and $V_{II}$). $V_I$: domain outside the fault zone, $V_{II}$: domain within the fault zone, $S_2$: boundary at which traction is applied, $\mathbf{q_b}$: traction, γ: body force.

and it can be simulated by reducing the shear modulus of the fault material. The slip observed on the ground surface can be used as a constraint in determining the degree to which the shear modulus should be reduced.

According to the principle of virtual work, the equation for the tectonic stress field before fault slip can be given as

$$\int_V \tilde{\boldsymbol{\varepsilon}}^{\mathbf{T}} \boldsymbol{\sigma}_{\mathbf{0}}\, dV = \int_V \tilde{\mathbf{u}}^{\mathbf{T}} \gamma\, dV + \int_{S_2} \tilde{\mathbf{u}}^{\mathbf{T}} \mathbf{q_b}\, dS \tag{1}$$

and the equation for the displacement field caused by the tectonic stress field and material softening can be determined as

$$\int_V \tilde{\boldsymbol{\varepsilon}}^{\mathbf{T}} \mathbf{D} \Delta\varepsilon\, dV = \int_{V_{II}} \tilde{\boldsymbol{\varepsilon}}^{\mathbf{T}} \Delta \mathbf{D}^{II} \boldsymbol{\varepsilon}_{\mathbf{0}}^{II}\, dV \tag{2}$$

where $V = V_I + V_{II}$ represents the solution region; subscripts I and II denote the domains outside and inside the fault, respectively (Fig. 1); $\tilde{\mathbf{u}}$ and $\tilde{\boldsymbol{\varepsilon}}$ are the virtual displacement and virtual strain, respectively; $\boldsymbol{\sigma}_{\mathbf{0}} = \mathbf{D_0}\boldsymbol{\varepsilon}_{\mathbf{0}}$ is the initial stress field before slip along the fault, where $\mathbf{D_0}$ is the elastic material matrix and $\boldsymbol{\varepsilon}_{\mathbf{0}}$ the strain before slip along the fault; γ is the body force due to gravity; $\mathbf{q_b}$ is the tectonic stress applied to the boundary $S_2$ (Fig. 1); $\mathbf{D}$ is the elastic material matrix after slip along the fault; $\boldsymbol{\Delta\varepsilon}$ is the change in strain caused by slip; and $\boldsymbol{\Delta D}$ is the change in the elastic material matrix in the fault. The displacement, strain, stress, and force mentioned above are given as vectors. Formula (1) can be developed further into the following finite element formula for the initial displacement field $\mathbf{U_0}$ caused by γ and $\mathbf{q_b}$ before slip along the fault:

$$\mathbf{K_0 U_0} = \mathbf{F_0} \tag{3}$$

where $\mathbf{K_0}$ is the global stiffness matrix in the region V, and $\mathbf{F_0}$ is the global nodal load vector. These values are derived from the body force and boundary force, respectively:

$$\mathbf{K_0} = \sum_{e=1}^{m+n} \int_{V^e} \mathbf{B}^{\mathbf{T}} \mathbf{D_0} \mathbf{B}\, dV^e,$$

$$\mathbf{F_0} = \sum_{e=1}^{m+n} \left( \int_{V^e} \mathbf{H}^{\mathbf{T}} \gamma\, dV^e + \int_{S_2} \mathbf{H}^{\mathbf{T}} \mathbf{q_b}\, dS_2^e \right)$$

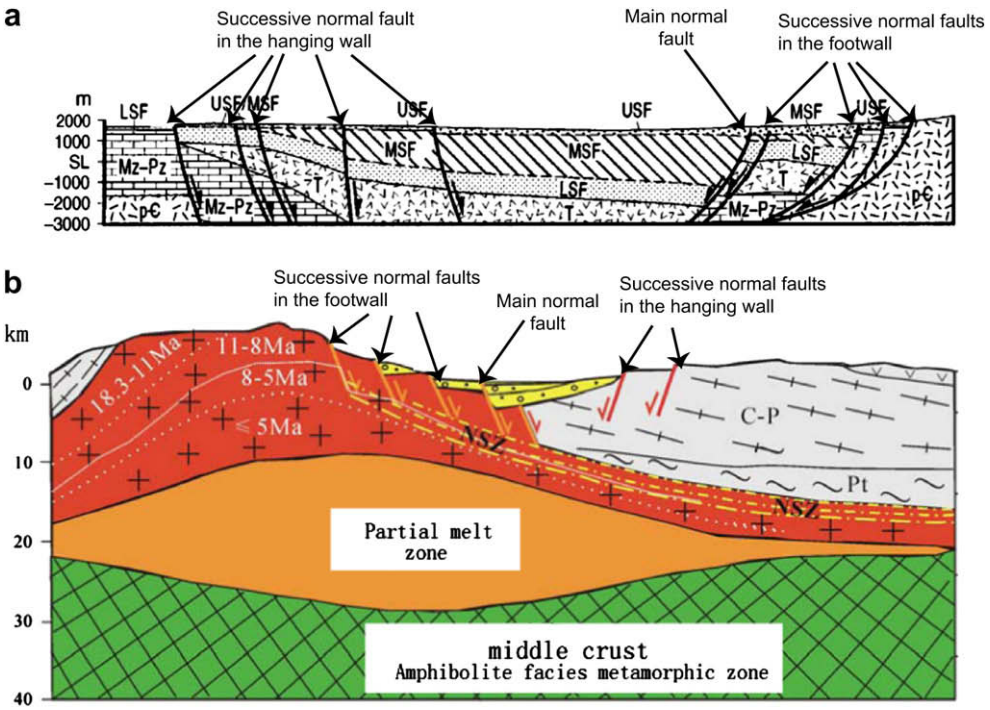


**Fig. 2.** Examples of geological cross-sections across normal faults. a) Cross-section through the Rio Grande rift. Pre-rift units: p–C = Precambrian, Mz–Pz = Mesozoic and Paleozoic. Synrift units: T = older Tertiary, LSF = Lower Santa Fe Group, MSF = Middle Santa Fe Group, USF = Upper Santa Fe Group. SL: sea level (after Mozley and Goodwin, 1995). b) Cross-section through the Damxung-Yangbajain graben (after Wu, 2005).

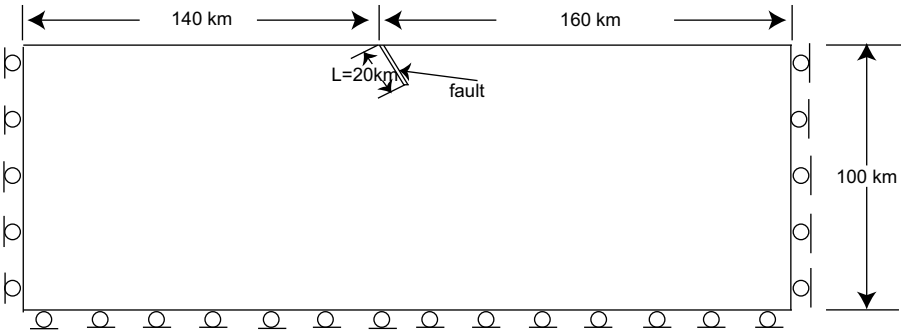


**Fig. 3.** Details of the finite element model employed in this study.

where m and n are the number of elements outside and inside the fault, respectively; **H** is the shape function matrix; and **B** is a connection matrix between strain and displacement (Cai, 1997).

Formula (2) can be used to construct the following finite element formula for solving the displacement change **ΔU** caused by the displacement field $\mathbf{U_0}$ and material softening in the fault:

$$\mathbf{K\Delta U} = \mathbf{\Delta F} \tag{4}$$

where **K** is the global stiffness matrix in the analyzed region V and **ΔF** is the nodal load vector related to the nodal displacement $\mathbf{U_0}$ (outside the fault, $\mathbf{\Delta D} = 0$):

$$\mathbf{K} = \sum_{e=1}^{m+n} \int_{V^e} \mathbf{B^T D B}\, dV^e, \quad \mathbf{\Delta F} = \sum_{e=1}^{n} \int_{V_{II}^e} \mathbf{B^T \Delta D B U_0^e}\, dV_{II}^e \tag{5}$$

The FEM is based on Formulae (2) and (4). The remarkable feature of Formulae (2) and (4) is that the change in strain or displacement caused by slip along the fault is related to the initial strain or displacement and the change in the elastic material matrix within the fault. This overcomes the shortcoming in previous numerical methods, in which fault slip was independent of the initial displacement or stress field (Melosh and Williams, 1989). This approach can also be used to study the stress changes that result from numerous slip events, and the progressive evolution of the stress field.

The simulation of fault slip by the FEM is achieved in two steps. First, the initial displacement field due to the effect of the body force and the boundary force is solved by Formula (3); the initial displacement field is always inhomogeneous as a result of the complexity of the fault geometry, the effect of gravity, etc. Second, the fault slip is calculated using Formula (4), and by reducing the shear modulus of the material in the fault. The stress fields before and after slip along the fault can be calculated using the initial displacement field $\mathbf{U_0}$ and the displacement field after slip, where $\mathbf{U} = \mathbf{U_0} + \mathbf{\Delta U}$. The displacement and stress fields after slip become the initial displacement and stress fields to be used when considering the next slip event upon the fault.

## 3. FEM model of normal faulting

Geological and seismic studies show that normal fault systems are commonly complex and composed of several faults (Fig. 2). A succession of normal faults develop in a regular arrangement in the hanging wall and footwall subsequent to the initiation of the main normal fault, and their slip directions may be either the same as or different from the slip direction of the main fault. How does such a system develop? To answer this question requires an understanding of the characteristics of the displacement and stress fields induced by slip along the main normal fault.

### 3.1. Geometry and materials of the FEM model

If the length of the normal fault zone is much greater than its width, the problem of fault slip in three dimensions can be simplified to that of plane strain. The dimensions of the model considered here, and within which the fault is set, are 300 km in the horizontal and 100 km in the vertical (Fig. 3). The fault zone itself has a dip of 60°, thickness of 250 m, and it extends along the dip direction for 20 km (Scholz, 2002).

The material in the fault zone can be described by layered material with five independent parameters: Young's modulus $E_1$

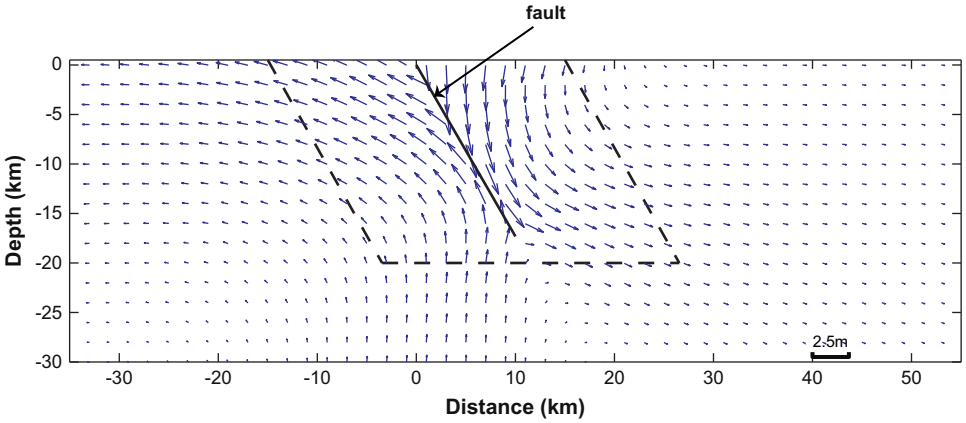


**Fig. 4.** Details of the displacement vector field obtained in this study.

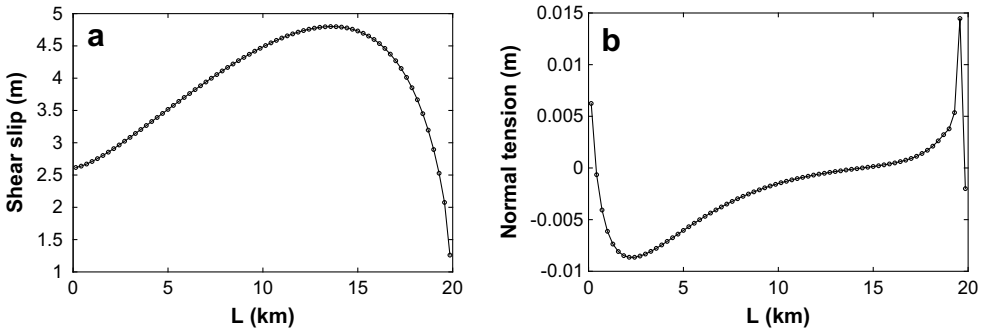


**Fig. 5.** Relative displacements along the modeled fault. a) Shear slip. b) Normal slip.

and Poisson's ratio $v_1$ for the fault plane, and Young's modulus $E_2$, Poisson's ratio $v_2$, and the shear modulus $G_2$ normal to the fault plane. The material outside the fault zone is regarded as isotropic, and the values given for $E$, $v$, and the density $\rho$ are the average values for the upper crust (76.6 GPa, 0.2474, and 2656 kg/m$^3$, respectively). Before slip along the fault, Young's modulus within the fault zone is the same as that outside the zone, so that $E_1 = E_2 = E$ and the Poisson's ratio $v_1 = v_2 = v$. The shear modulus $G_2$ normal to the fault plane within the fault zone is smaller than that outside, and initially $G_2 = 5$ GPa (Gudmundsson, 2004).

### 3.2. Boundary conditions of the FEM model

In the FEM model, the ground surface is free, and there is no shear stress and normal displacement on the other three boundaries (Fig. 3). According to the assumption of plane strain, the vertical and horizontal stresses produced by gravity should be $\rho gh$ and $\rho ghv/(1-v)$, where $\rho$ is density, $h$ is depth, $g$ is acceleration due to gravity, and $v$ is Poisson's ratio. Therefore, on the vertical and lateral boundaries of zero normal displacement, the reactive pressures are equal to $\rho gh$ and $\rho ghv/(1-v)$, provided the boundary conditions are released. Thus, the maximum and minimum principal stresses are $\rho gh$ and $\rho ghv/(1-v)$, respectively. The boundary conditions ensure that the stress field in this model can produce a normal fault.

## 4. Numerical results

The code for the FEM used in this paper was developed using the software FEPG (Finite Element Program Generator) provided by the Feijian Company, China. The numerical results obtained by the FEM simulation are given in the following sections.

### 4.1. Displacement field due to fault slip

#### 4.1.1. Displacement field outside the fault zone

Fig. 4 shows the displacement vector field that develops outside the fault zone as a result of normal fault slip. Significant displacements are mainly distributed within a region of 30 km wide and 20 km deep; displacement decreases away from the fault. The maximum displacement is along the lower part of the fault, not near the top. From the ground surface to a depth of 10 km, downward vertical components of displacement are prevalent in the hanging wall; horizontal components gradually dominate below a depth of 10 km. Not only are the displacements within the footwall region different from those in the hanging wall, but also the directions of movement differ. Near the surface, displacement directions in the footwall region approach horizontal, and the magnitude of displacement decreases away from the fault. Within the footwall region, at the lower end of the fault, the displacement directions are almost vertical.

#### 4.1.2. Distribution of displacement along the fault

Fig. 5 shows the relative displacement along the fault. The values of shear slip in Fig. 5a reveal differences in shear displacement on the footwall and hanging wall. The hanging wall slips downwards if shear slip is positive. Shear slip is not uniform: the maximum values lie within the lower part of the fault. Fig. 5b shows values of normal tension, which is the difference between the

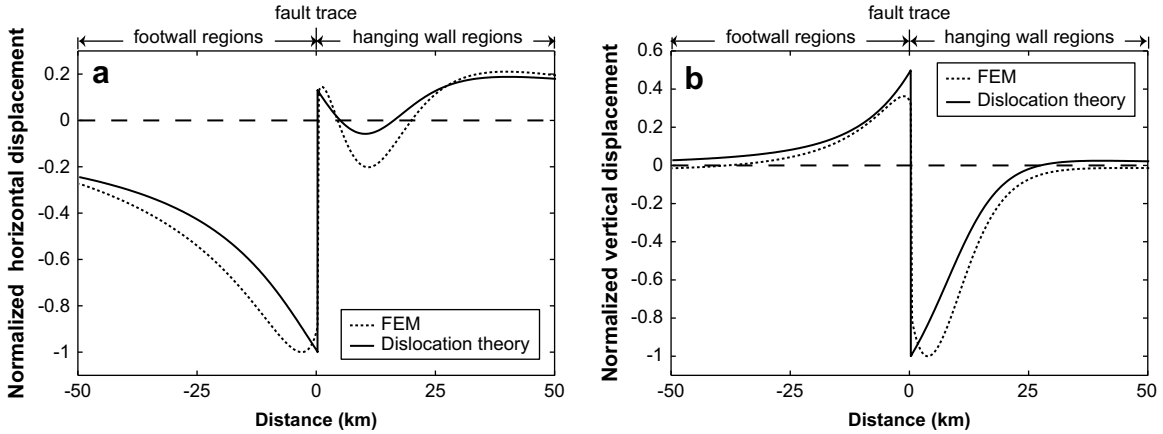


**Fig. 6.** Distribution of displacement upon the ground surface. a) Horizontal displacement. b) Vertical displacement. The fault trace position coincides with distance of 0 km on this diagram, the left-hand sides of (a) and (b) represent the footwall regions, and the right-hand sides represent the hanging wall regions.

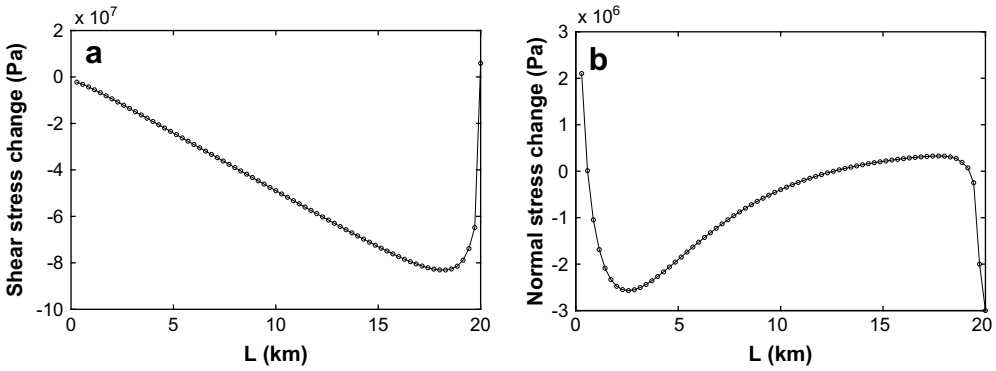


**Fig. 7.** Stress change within the fault zone during fault slip. a) Change in shear stress. b) Change in normal stress.

normal displacement on the footwall and hanging wall surfaces. Negative values indicate compression, positive values tension. The fault zone will extend if normal tension is positive. The fault zone is in tension at the surface, but rapidly enters compression with increasing depth before returning to tension in the lower part of the fault zone and compressive once again at the termination of the fault. Maximum compression occurs at around 2 km depth. Both the shear slip and normal tension differ from those in seismic dislocation theory, which specifies shear slip on the fault surface in advance, and sets normal tension to zero.

*4.1.3. Distribution of displacement upon the ground surface*

For a better comparison between the results of the FEM modeling and dislocation theory, the displacements are normalized to the maximum displacement. Fig. 6 shows the normalized displacements on the ground surface due to slip upon the fault: Fig. 6a shows the normalized horizontal displacements, and Fig. 6b the normalized vertical displacements. The maximum horizontal and vertical displacements are found on the footwall and hanging wall sides, respectively, and the locations of maximum ground displacement lie away from the fault. This finding differs from the results of seismic dislocation theory, in which the maximum displacement coincides with the position of the fault. In Fig. 6a, the horizontal displacement within the footwall monotonously decreases to the left, away from the fault; however, its distribution within the hanging wall region is more complicated. From the top of the fault line towards the right, positive displacement values indicate tension, as also observed in the area furthest from the fault line; however, a middle zone is assigned negative values that represent compression. In Fig. 6b, the downward displacements within the hanging wall region and upward displacements within the footwall region show a monotonous decrease with increasing distance from the fault. The ground surface displacements are close to zero at about 50 km from the fault.

*4.2. Stress field due to fault slip*

*4.2.1. Stress changes in the fault zone*

Fig. 7 shows changes in shear stress with depth along the fault plane, and changes in normal stress due to the slip upon the fault; increasing negative values of change in shear stress indicate a drop in shear stress, and negative values of normal stress indicate compression, positive values tension. In Fig. 7a, the shear stress drop shows an approximately linear increase with depth. The maximum shear stress drop is found near the lower end of the fault. Fig. 7b shows the fault zone in tension near the ground surface and to a depth of 500 m, where it enters compression with increasing depth; much of the lower part of the fault is in tension, but the lowermost end of the fault is again in compression. These values are consistent with the distribution of relative displacement along the fault (Fig. 5). The magnitude of shear stress change exceeds that of normal stress change. It is noteworthy that the maximum shear stress drop and maximum shear slip occur at different locations upon the fault.

*4.2.2. Stress changes outside the fault zone*

Fig. 8 shows the distribution of stress change outside the fault zone (the lines in the figure indicate no change in stress). The pattern of shear stress change shown in Fig. 8a is clearly symmetrical about the fault, and can be described in terms of three regions. In the smallest region, within 5 km of the ground surface, the shear stress increases, indicating an increase in the risk of shear failure. The second region, which extends from about 5 to 17 km depth, is characterized by a decrease in shear stress, meaning that shear

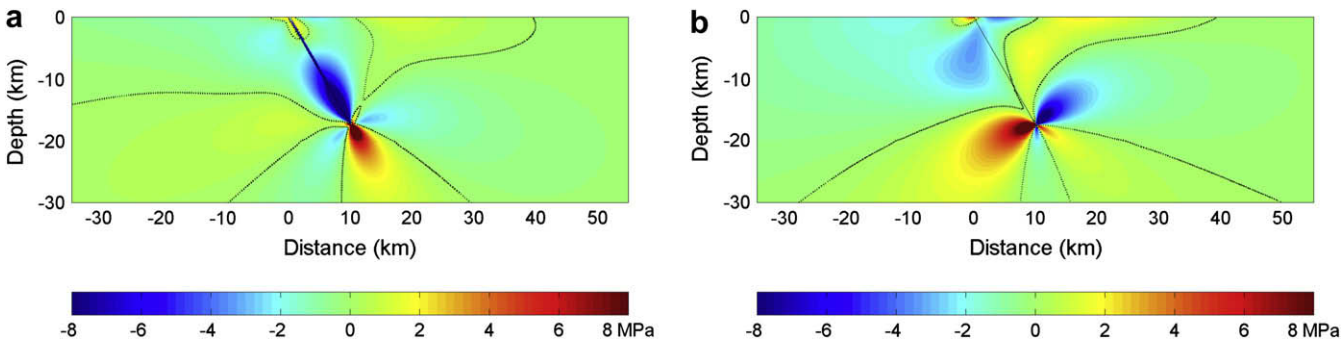


**Fig. 8.** Stress change outside the fault zone during fault slip. a) Change in shear stress. b) Change in normal stress.

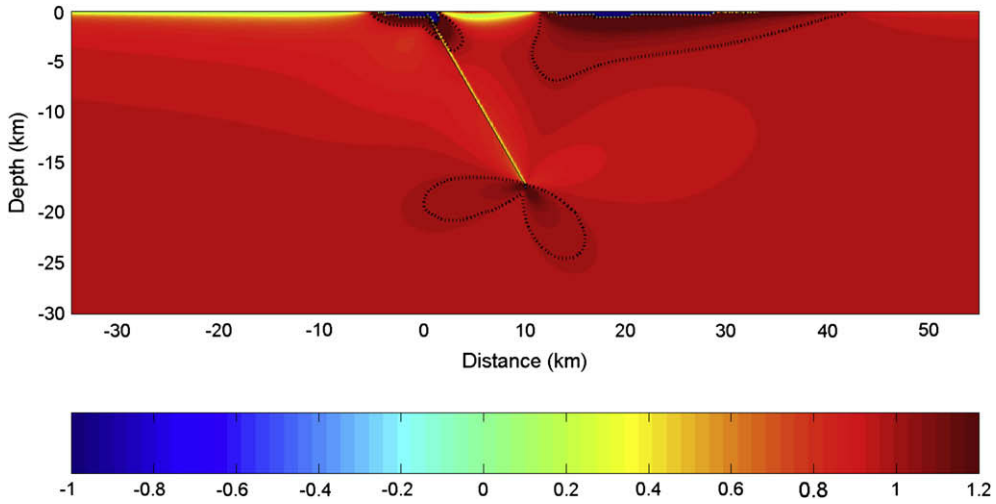


**Fig. 9.** Areas of failure arising from fault slip.

failure is unlikely. The third and largest region consists of three leaf-shaped areas at angles of 120° to each other, within which the shear stress increases.

All three areas meet near the lower end of the fault. The first area is characterized by the highest shear stress increase, and is largely aligned with the fault itself. One of the other areas lies in the footwall and does not reach the surface; the third area lies in the hanging wall and reaches the surface. The strong increase in shear stress in the first area indicates that new shear failures will readily develop, leading to a down-dip extension of the fault, as already well known from seismic dislocation theory. However, more attention should be paid to the area in the hanging wall where a zone of increased stress reaches the surface from the lower end of the fault; it is possible that long bands of shear failure might initiate in this region.

Fig. 8b shows the normal stress change in the direction perpendicular to the fault (positive values indicate a decrease in compressive stress or material in tension, and negative values indicate an increase in compressive stress or material in compression). There occurs a remarkable tensile region in the footwall near the fault top, and tensile failures have been found during geological surveys in this area (Gudmundsson, 1987a,b). Three other tensile areas are arranged in the shape of three leaves that meet at the end of the fault. The first area extends downward sub-parallel to the fault; the second is developed in the footwall and does not reach the surface; and the third area, within the hanging wall, extends upwards to reach the surface. It is notable that most of the hanging wall zone falls in an area where the shear stress increases and compressive stress decreases, thereby favoring the development of shear failure. In fact, this is the area in which a succession of normal faults usually develops.

### 4.3. Failure regions due to slip along the fault

To study the development of failure regions arising from slip along the normal fault, we employ the Coulomb failure factor $D$, which is the ratio of shear stress $|\tau_n|$ to frictional strength $\mu\sigma_n$ on a slip surface, with n being the normal direction. $D = -|\tau_n|/(\mu\sigma_n)$, where $\mu$ is the internal coefficient of friction, which is taken as 0.6 in this study. $\sigma_n$ is the normal stress (tensile stress is positive) on the slip surface. When the normal stress $\sigma_n$ is compressive, $D$ is positive. $D \geq 1$ means that Coulomb failure occurs. When the normal stress $\sigma_n$ is tensile, $D$ is negative. Because the tensile strength of rock is much less than its frictional strength, rock is considered to have no resistance to tensile stress. $D < 0$ indicates tensile failure. When $\sigma_n$ is the tensile stress, tensile failure will occur first.

The obtained failure regions are shown in Fig. 9 (Coulomb shear failure occurs in the regions enclosed by the dash lines). There are two notable failure regions where $D > 1$ near the ground surface. The first is close to the fault itself, with the failure region in the footwall being larger than that in the hanging wall. The second region starts about 12 km from the fault, and is located in the hanging wall. Its shape is similar to that of a right-angle triangle, and this region is larger than the first. The location of these failure regions explains why a succession of normal faults may form at these sites. Between the two failure regions there exists a non-failure region in which the shear stress decreases; in the geological example shown in Fig. 2 there are no normal faults in this region. There are two areas of tensile failure where $D < 0$, located above the two failure regions, and the maximum depths of these areas, moving away from the hanging wall of the fault, are about 1.8 and 1.5 km. This finding suggests that the formation of normal faults (in regions of Coulomb failure where $D > 1$) starts from regions of tensile failure near the ground surface, thereafter extending downwards. This process has been verified in field studies (Gudmundsson, 1987a,b) and theoretical modeling (Gudmundsson, 1992). The third region of Coulomb failure in which $D > 1$ is located near the lower end of the fault, consisting of two leaf-shaped areas in which shear failure is expected to occur.

## 5. Conclusions and discussion

The results obtained from the FEM simulations differ from those predicted by seismic dislocation theory. Our analysis revealed the following findings: 1) the maximum slip along the fault plane is observed in the lower part of the fault, not at the top; 2) the locations of the maximum horizontal and vertical displacements on the ground surface do not coincide with the fault trace; 3) the maximum shear stress drop and the maximum shear slip along the fault are not found at the same location; 4) near the ground surface, slip along the normal fault leads to the development of two regions of Coulomb failure, in which a succession of normal faults may develop; a region without Coulomb failure also forms close to the fault on the hanging wall side, and normal faults are not expected to develop here; 5) the complexity of normal fault

systems can be regarded to arise from the occurrence of many failure events and the development of a succession of normal faults.

In this paper, we discussed the influence of a heterogeneous tectonic stress field on the development of normal fault systems, and provided mechanical explanations of these phenomena based on a conceptual model. Although the results help to explain the characteristics of some normal fault systems, they do not explain the features of all normal fault systems, especially those that develop over long periods of time within changing stress systems.

## Acknowledgments

We would like to thank the Journal reviewers A. Gudmundsson and K. Mulchrone for insightful comments, A. Stallard for improvement of the English, and Zhen-Han Wu for his helpful discussions and comments. This work was supported by NSFC grants 40474013, 40821062 and the Special Research Project in Earthquake Science, CEA (200808068).

## References

Aagaard, B.T., Heaton, T.H., Hall, J.F., 2001. Dynamic earthquake failures in the presence of lithostatic normal stresses: implications for friction models and heat production. Bulletin of the Seismological Society of America 91 (6), 1765–1796.

Cai, Y.N., 1997. The Finite Element Method and Program Design of Thermo-elastic Problem (Chinese). Peking University Press, Beijing.

Caine, J.S., Evans, J.P., Forster, C.B., 1996. Fault zone architecture and permeability structure. Geology 24, 125–1028.

Chinnery, M.A., 1963. The stress changes that accompany strike-slip faulting. Bulletin of the Seismological Society of America 53, 921–932.

Colmenares, L., Zoback, M.D., 2003. Stress field and seismotectonics of northern South America. Geology 31 (8), 721–724.

Day, S.M., Yu, G., Wald, D.J., 1998. Dynamic stress changes during earthquake failure. Bulletin of the Seismological Society of America 88 (2), 512–522.

Evans, J.P., 1990. Thickness–displacements relationships for fault zones. Journal of Structural Geology 12, 1061–1065.

Gudmundsson, A., 1987a. Tectonics of the Thingvellir fissure swarm, SW Iceland. Journal of Structural Geology 9, 61–69.

Gudmundsson, A., 1987b. Geometry, formation and development of tectonic fractures on the Reykjanes Peninsula, southwest Iceland. Tectonophysics 139, 295–308.

Gudmundsson, A., 1992. Formation and growth of normal faults at the divergent plate boundary in Iceland. Terra Nova 4, 464–471.

Gudmundsson, A., 2004. Effect of Young's modulus on fault displacement. Comptes Rendus Geosicence 336, 85–92.

Gudmundsson, A., 2006. How local stresses control magma-chamber ruptures, dyke injections, and eruptions in composite volcanoes. Earth Science Reviews 79 (1–2), 1–31.

Hauksson, E., 1994. State of stress from focal mechanisms before and after the 1992 Landers earthquake sequence. Bulletin of the Seismological Society of America 84 (3), 917–934.

Li, Y.G., Aki, K., Vidale, J.E., Lee, William H.K., Chris, J.M., 1994. Fine structure of the Landers fault zone: segmentation and the failure process. Science 256, 367–370.

Li, Y.G., Aki, K., Vidale, J.E., 1999. 3-D Structure of the Landers Failure Zone from Trapped Waves and Seismic Measurements at the Punchbowl Fault. AGU annual report.

Li, Y.G., 2003. Characterization of failure zones at Landers and Hector Mine, California in 4-D by fault-zone guided waves. Earth Science Frontiers 10, 479–505.

Manshinha, L., Smylie, D.E., 1971. The displacement fields of inclined faults. Bulletin of the Seismological Society of America 61, 1433–1440.

Melosh, H.J., Williams Jr., C.A., 1989. Mechanics of graben formation in crustal rock: a finite element analysis. Journal of Geophysical Research 94, 13961–13973.

Mozley, P.S., Goodwin, L.B., 1995. Patterns of cementation along a Cenozoic normal fault: a record of paleoflow orientations. Geology 23 (6), 539–542.

Okada, Y., 1985. Surface deformation due to shear and tensile faults in a half-space. Bulletin of the Seismological Society of America 75, 1135–1154.

Okada, Y., 1992. Internal deformation due to shear and tensile faults in a half-space. Bulletin of the Seismological Society of America 82, 1018–1040.

Roman, D.C., Moran, S.C., Power, J.A., Cashman, K.V., 2004. Temporal and spatial variation of local stress fields before and after the 1992 eruptions of Crater Peak Vent, Mount Spurr Volcano, Alaska. Bulletin of the Seismological Society of America 94 (6), 2366–2379.

Schulz, S.E., Evans, J.P., 2000. Mesoscopic structure of the Punchbowl fault, Southern California, and the geologic and geophysical structure of active strike-slip faults. Journal of Structural Geology 22, 913–930.

Scholz, C.H., 2002. The Mechanics of Earthquakes and Faulting, second ed. Cambridge University Press, Cambridge.

Tamagawa, T., Pollard, D.D., 2008. Failure permeability created by perturbed stress fields around active faults in a failured basement reservoir. Bulletin of the American Association of Petroleum Geologists 92 (6), 743–764.

Wu, Z.H., 2005. The Atlas of Active Faults and Geological Disasters Along the Qinghai–Tibet Railway (Chinese). Earthquake Press, Beijing.

Xu, J.R., Zhao, Z.X., Yuzo, I., 2005. Extensional stress field in the central and southern Qinghai–Tibetan plateau and dynamic mechanism of geothermic anomaly in the Yangbajain area (Chinese). Chinese Journal of Geophysics 48 (4), 861–869.

Zoback, M.L., 1992. First-and second-order pattern of stress in the lithosphere: the world stress map project. Journal of Geophysical Research 97 (B8), 11, 703–11,728.